Development of broadband x-ray radiography for diagnosing magnetically driven cylindrically compressed matter

H. Sawada[1,a)], T. S. Daykin[1], T. M. Hutchinson[1], B. S. Bauer[1], V. V. Ivanov[1], F. N. Beg[2], H. Chen[3], G. J. Williams[3] and H. S. McLean[3]

[1] *Department of Physics, University of Nevada Reno, Reno, Nevada, 89557, USA*
[2] *Center for Energy Research, University of California San Diego, La Jolla, California, 92093, USA*
[3] *Lawrence Livermore National Laboratory, Livermore, California, 94550, USA*
a) hsawada@unr.edu

Experiments and modeling of x-ray radiography of millimeter diameter solid Al wires with laser-produced broadband x rays are reported. Experiments were performed using the 50-TW Leopard short-pulse laser in a laser and pulsed power chamber at the Nevada Terawatt Facility. To characterize broadband x rays and demonstrate a radiographic capability, bremsstrahlung, escaping electrons and radiograph images of Al wires were simultaneously measured. The angularly resolved x-ray spectra are modeled by comparing measured bremsstrahlung signals in the range between 10 and ~500 keV with hybrid particle-in-cell (PIC) simulations. Transmission of Al wires from the radiograph images is further simulated with a Monte Carlo code. The measured transmission profiles of Al wires with three different diameters agree with calculations when a simulated x-ray spectrum composed of line emissions and bremsstrahlung is used with a source size of 600 ± 200 μm. Transmission calculations with only 22 keV Ag Kα or an exponential x-ray spectrum do not reproduce the measurement, suggesting that the accurate determination of an x-ray source spectrum as well as inclusion of the photon sensitivity of the detector are critical in transmission calculation to infer the density of an object. The laser-based broadband x-ray radiography developed has been successfully implemented in a pulsed power chamber for future laser-pulsed-power coupled experiments.

I. Introduction

The interaction of intense short-pulse lasers with solid targets has been studied to develop bright x- and γ-ray sources for Inertial Confinement Fusion (ICF) and High Energy Density (HED) experiments.[1,2,3,4] The lasers with a peak intensity of > 10^{18} W/cm^2 can accelerate a large number of energetic electrons above MeV energies predominantly by the ponderomotive potential of the laser field. As the fast electrons transport through and recirculate around a solid target, characteristic x rays and bremsstrahlung are produced. Such secondary sources of radiations are used for characterization of fast electrons[5,6,7,8,9,10,11], positron generation[12], photon-nuclear reactions[13,14], and x-ray radiography[15,16,17,18]. A combination of laser-produced Kα and monochromatic crystal imaging has been applied as flash Kα radiography for diagnosing compressed cores of ICF targets[19,2021,22,23,24].

To obtain radiographs of high-density or high areal density objects, broadband x-ray sources are required since the energy of Kα photons and Kα crystal imaging is limited to 80 keV and ~25 keV[25], respectively. In particular, high energy broadband x rays are essential to diagnose high-density ICF cores that produce strong self-emission during the implosion. Typical thermal emission from low-Z capsule implosions is continuum with x-ray energies up to ~ 20 keV. The use of a broadband x-ray backlighter between 40 and 200 keV allows for strongly attenuating the self-emission with a high pass filter.[26] To accurately infer the density of an object from recorded images, knowledge of the x-ray source spectrum is critical for broadband x-ray radiography.

The Nevada Terawatt Facility (NTF) has developed a simultaneous capability using the 50-TW Leopard laser and a 2 Mega-Ampere (MA) pulsed power generator Zebra in the same vacuum chamber.[27] This unique capability at a university-scale facility offers various experimental configurations such as generation of magnetic fields for magnetized laser-plasma experiments[28], ionization state measurements of pulsed-power produced plasmas[29], study of laser-produced plasmas in strong magnetic field[30], and laser-produced proton deflectometry for magnetic field measurement[31]. Taking advantage of this coupled capability, we have proposed magnetically driven cylindrical compression to create strongly coupled matter.[32] Magnetic fields produced by a slow-rise MA current pulse can isentropically compress matter.[33] A Magnetohydrodynamic (MHD) simulation predicts that a 1 mm diameter Al wire can be compressed with a 80 ns rise-time, 1 MA Zebra current to warm dense matter/a strongly coupled plasma in the range of a few eV and several times solid density. To probe such a large volume of dense plasmas, a hard x-ray source above 10 keV is required.

Here, we report development of broadband x-ray radiography of mm-diameter Al wires with laser-produced x rays. In our laser experiment, the x-ray source spectrum is characterized by comparing angularly-resolved bremsstrahlung measurements with hybrid particle-in-cell modeling. Subsequently, measured transmission profiles through various Al wire diameters are modeled with a Monte Carlo code. Comparisons of the measured and simulated transmission profiles allow us to determine the x-ray source size and spectrum. The experimental transmission is reproduced when both bremsstrahlung and characteristic line emissions are included in the simulation. The radiographic technique developed was further applied for probing a 1 mm Al wire load in a pulsed power vacuum chamber, as will be discussed in Sec.5.

II. Experiment

A broadband x-ray radiography experiment was carried out using the 50-TW short-pulse Leopard laser at the NTF[27]. Figure 1(a) shows a schematic of the experimental layout from the top view. The Leopard laser delivered a 0.35 ps Gaussian pulse (FWHM) with an energy up to 15 J. The beam was focused with a f/1.5 dielectric-coated off-axis parabolic (OAP) mirror down to a 8 μm diameter spot size containing 30% of the laser energy[34], achieving a peak laser intensity of ~ 1×10^{19} W/cm^2. The laser was incident on the foil at 30° from the target normal. The thickness of silver foils was varied from 10 to 100 μm, while the surface area was maintained between 500×500 μm^2 and 700×700 μm^2. Figure 1(b) shows a photograph of a silver foil mounted on a glass stalk. Since the foils were manually cut and mounted with glue, not only the surface area of the foil, but also the angle of the foil with respect to the stalk varied from target to target. We selected and used targets having the titled angle less than 15°.

Fast electrons produced in the laser-foil interaction recirculate around the foil due to sheath potentials, resulting in continuous production of line emissions and bremsstrahlung over tens of picoseconds. Bremsstrahlung was measured with differential filter stack spectrometers[35] at two angular positions (Brems1 at 180° and Brems2 at 270°). Magnets were placed to divert electrons from going into the bremsstrahlung spectrometers. Escaped fast electrons were recorded with a magnetic spectrometer (e-spec)[36] along the laser axis. The slope of the fast electrons, which is a direct indication of on-target laser intensity[37], was used to monitor shot-to-shot variations due to target misalignment or changes in the laser energy.

Using the broadband x rays produced from the Ag foil, x-ray radiographs of cold solid Al wires (1100 Al wire from McMaster) were recorded on image plates (IP) in point projection geometry[38]. Fig. 1(c) displays a photograph of the Al wires with diameters of 0.5, 1.0 and 1.6 mm glued onto a 10 mm thick polyethylene (C_2H_4) piece. The CH piece acts as a high pass filter to cut photons below 10 keV. Each IP was placed at the back end of a 20 cm long, 1 cm thick aluminum collimator[39] and closed by a 2 cm thick CH cap. The entrance of the collimators was covered by a 25 μm thick aluminized Mylar for protecting the IPs from visible light.

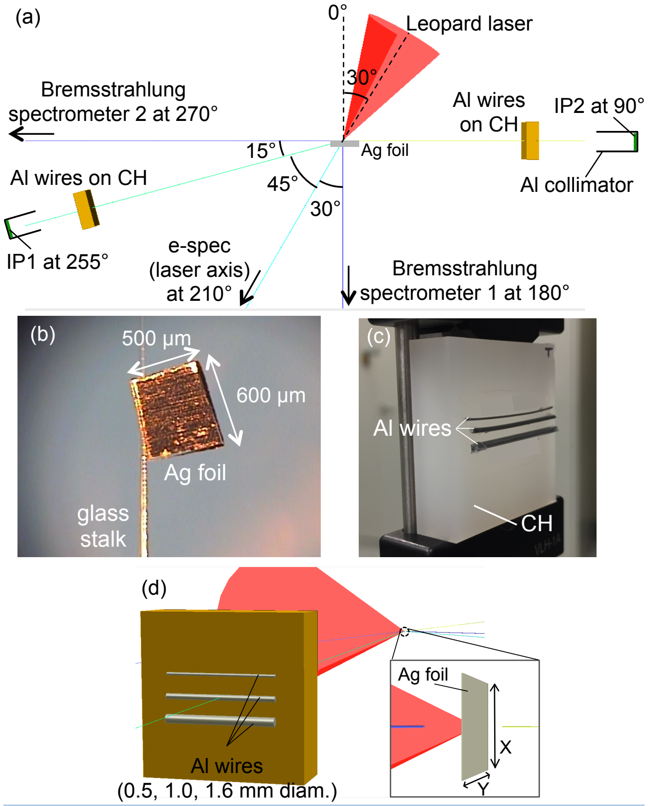

Figure 1 (a) A schematic of the x-ray characterization and radiography experiment. The incident angle of the laser is 30°. (b) A photograph of a silver foil target (target 17). (c) A photograph of Al wires glued on a polyethylene (CH) filter. (d) 3D CAD drawing of the experiment. The inset shows a view from the behind of the CH filter in the direction to the Ag foil.

Two sets of the radiograph package (3 Al wires on a CH filter and IP) were fielded at 255° (IP 1) and 90° (IP 2). The CH filters and IPs were positioned at 21.6 cm and 78.7 cm for IP 1, and 15.2 cm and 76.2 cm for IP 2, respectively. The magnifications of the wire radiography were ~3.6 and ~5 at IP 1 and IP 2. Fig. 1(d) shows a 3D CAD drawing view from the radiograph package of IP 1 and the inset of Fig.1 (d) shows the target foil orientation. From this view angle, a 500 μm^2 Ag foil appears to be 129 μm [500 μm×cos(75°)] in Y, whereas the height of the foil is same as the initial 500 μm in X.

Figure 2 shows measurements of escaped fast electrons, bremsstrahlung and x-ray radiographs of the Al wires on a single shot (shot13). The slope of the electron spectrum is fit with an exponential function to be 0.59 ± 0.05 MeV. As shown later, this information on the slope temperature is used to verify the slope of an electron spectrum inferred from analysis of bremsstrahlung measurements. Fig. 2(b) shows bremsstrahlung signals recorded on each IP layer in

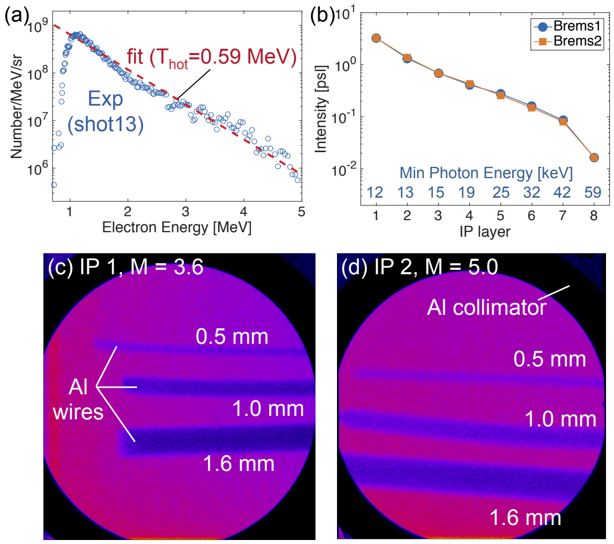

Figure 2 (a) Measured escaped electron spectrum with an exponential fit of 0.59 ± 0.05 MeV. (b) Experimental bremsstrahlung spectrometer signals. X-ray images of Al wires using the bremsstrahlung x-ray source at (c) IP 1 and (d) IP 2. The two images are displayed in the same color scale, but the magnification is 3.6 and 5.0 for IP 1 and IP 2, respectively.

the spectrometers. This diagnostic consists of 15 layers of IPs and metal filters.[35] However, the signals recorded in this experiment were only up to the 8th layer. The first 8 metal filters and thicknesses are layers of 100 μm Al, 100 μm Ti, 100 μm Fe, 100 μm Cu, 100 μm Mo, 150 μm Ag, 500 μm Sn and 500 μm thick Ta.[40] The minimum energy of photons that can penetrate through each filter is shown in Fig. 3(c). The bremsstrahlung signals recorded at the two angular positions show no angular dependence (i.e., isotropic), even though our previous experiment reported by Daykin[41] showed an anisotropy of bremsstrahlung produced by the same laser system. This inconsistency can be explained by the lower fast electron temperature in the present work than the past experiments[11,41]. The fast electron slope temperature shown in Fig. 2(a) is ~0.6 MeV, whereas it was ~1.5 MeV in the past experiments. The lower slope temperature indicating low peak intensity also explains the weak bremsstrahlung signals only up to the 8th layer in this work. The low peak intensity could be attributed to lower laser energy delivering to the target due to damages in the mirrors and OAP in the laser chain over the course of time since the experiment reported here was carried out in 2018 and the others were in 2013.

Fig. 2(c) and (d) show x-ray radiographs of Al wires at the position of IP 1 and IP 2. Recording radiographs of three wires with different diameters on a single IP can strongly constrain the spectrum of x rays, namely transmissions of the wires must simultaneously match a single x-ray spectrum in modeling. Fielding two radiograph packages at different angular positions are a valuable method to provide information on angular dependence of the x-ray source sizes.

III. Modeling of fast electron-induced broadband X rays using a hybrid-PIC code LSP

Broadband x rays generated by fast electron transport in a 10 μm thick silver foil are simulated with a hybrid-PIC code Large Scale Plasma (LSP)[42]. The simulations are performed in a 2D Cartesian coordinate system by injecting fast electrons at an incident angle of the laser beam and no laser-plasma interaction is solved. Figure 3(a) shows the simulation geometry of a 10 μm thick Ag foil. A beam of fast electrons is injected at Z=0 with at an incident angle of 30° within a 20 μm diameter beam spot that. This larger beam spot than the laser spot at the foil surface is due to a consideration of a divergence of fast electrons generated by the 8 μm laser spot in a preplasma. It is noted that calculated angularly resolved x-ray spectra mainly depend on the choice of electron spectrum and electron divergence angle because of strong electron recirculation, and are insensitive to the variation of the beam spot diameter. Simulations include developments of self-generated fields during the electron transport. Simulation parameters varied are: slope temperature of the fast electron energy spectrum (T_{hot}) and electron injection half-angle (θ). Changes in the total injected energy only vary the total electron number so that simulated x-ray spectra simply scale with the energy in the simulation regime we considered for this experiment (i.e., <15 J laser energy). Dependence of the injected energy on the spectrum intensity, therefore, is cancelled out when the simulated spectrometer signals are normalized for comparing to measurements. The transverse spread of the injected electrons is described using a Gaussian function. The simulation box size is 0.8 mm x 0.8 mm with a cell size of 2 μm in each dimension, and all simulations are run up to 20 ps. The time step is determined in the code by using a Courant multiplier of 0.5.

Figure 3(b) shows x-ray spectra calculated with T_{hot} = 0.5 MeV and θ = 15° in the direction of Brems1 (180°), Brems2 (270°) and IP1 (255°). The spectra show 22 keV Ag Kα, 25 keV Kβ and bremsstrahlung. The x-ray spectra above ~70 keV are similar for the three cases and are fit well with an exponential function of 80 keV. The ratio of the Kα photons to the total number of bremsstrahlung between 10 and 100 keV excluding the Kα is 0.49, 0.53 and 0.50 for Brems1, Brems2 and IP 1, respectively. To compare the simulations to the bremsstrahlung measurements, the simulated x-ray spectra are post-processed using filter response function calculated with a Monte Carlo code, Particle and Heavy Ion Transport System (PHITS)[43]. The filter responses are updated in this work from the original spectrometer design[7] calculated with a 1D Monte Carlo code ITS 3.0[44] by incorporating the benchmarked IP information in the PHITS calculation. We confirmed that our PHITS modeling of the photon and

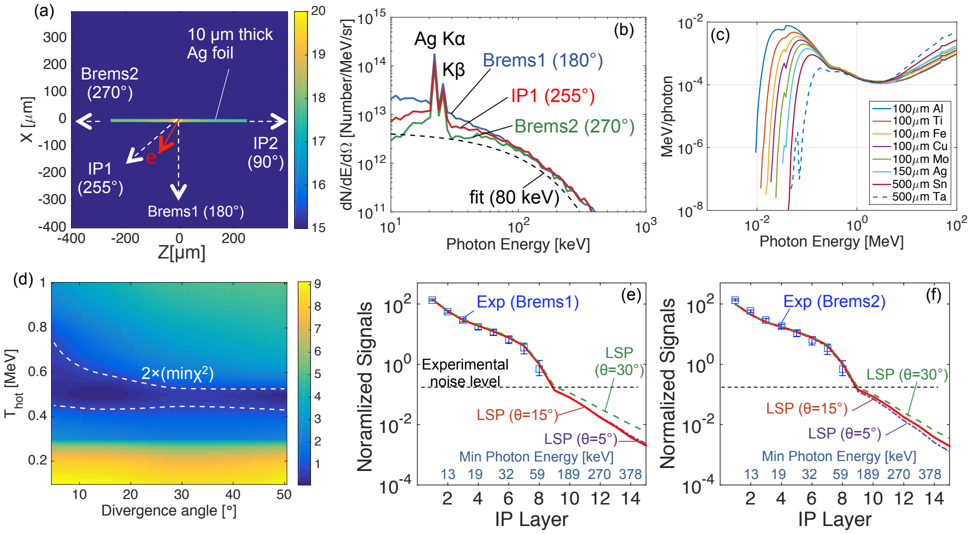

Figure 3 (a) A target geometry and diagnostic positions with respect to the target in a 2D Cartesian LSP simulation. The contour in the foil shows x-ray intensity distribution above 100 keV. (b) Simulated x-ray spectra in the directions of Brems1 (180°), Brems2 (270°) and IP1(255°). (c) Filter response function of IPs after each metal filter up to the 8th layer. (d) a contour of χ^2 map for the fit. Comparisons of simultaneous fit to the measured bremsstrahlung spectrometer signals for (e) Brems1 and (f) Brems2.

electron sensitivities of the IP agree with published results[45,46]. Figure 3(c) shows the response function of IPs after each metal filter up to the 8th layer. Each photon is deposited in the IP corresponding to its energy. Spectrometer signals are calculated by accumulating the dose contributed from all photons at each layer. More detail of the conversion from the spectrum to spectrometer dose and fitting procedure is described in our previous publication[41].

The two-bremsstrahlung signals are simultaneously fit with a series of LSP simulations by varying T_{hot} and θ in the range of $0.1 \leq T_{hot} \leq 1.0$ MeV and $5° \leq \theta \leq 50°$. A best fit is found to be $T_{hot} = 0.59 \pm 0.15$ MeV from a χ^2 analysis shown in Fig. 3(d). The slope temperature inferred from

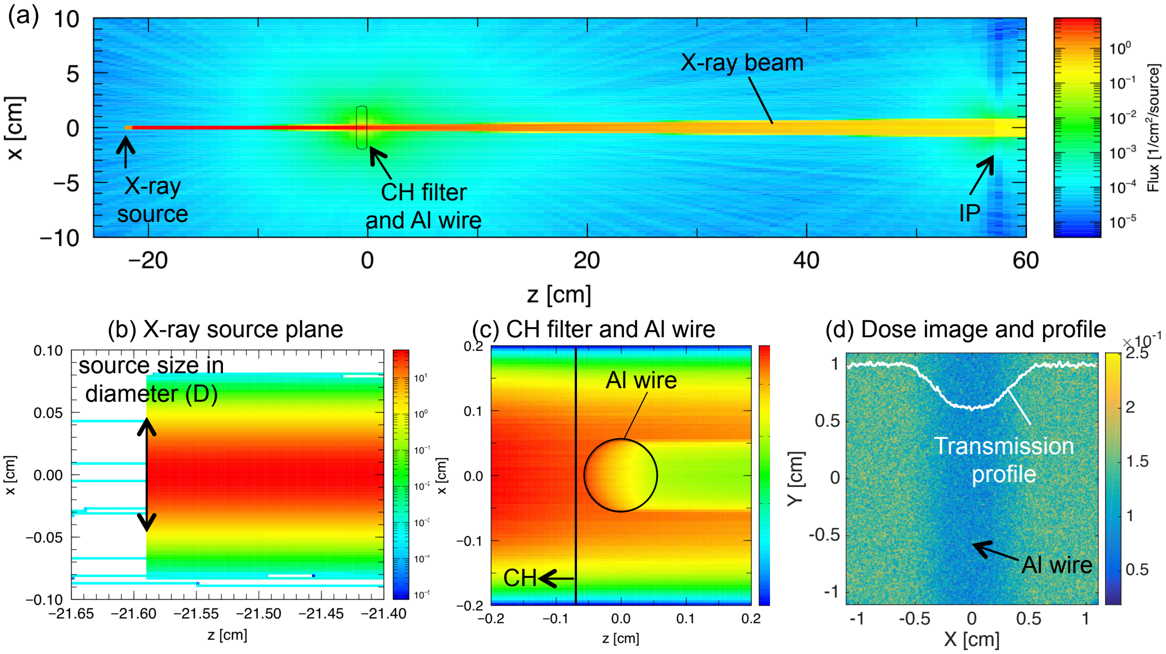

Figure 4 (a) A setup of a PHITS simulation (side view). Close-up views of (b) the x-ray source plane at Z=-21.6 cm and (c) a CH filter and Al wire at Z=0. (d) Dose image in the phosphor layer of the IP and transmission profile at Z=58 cm.

this analysis agrees with T_{hot} from the direct electron measurement, which is consistent with the past result[41]. Fig. 3(e) and (f) show comparisons of the measurements and simulations using T_{hot} = 0.50 MeV with θ =5°, 15° and 30°. The measured and simulated spectrometer signals are normalized to the signal at the 8th layer. The experimental data agree with the simulations for all three cases, implying that the present data sets cannot constrain the divergence angle. It is noted that the simulations show variations in the spectrum with the divergence angle only in the deeper layer (>9th layer) or above 100 keV photons in Fig. 3(e) and (f). As will be shown later, calculated transmission profiles through millimeter diameter Al wires depend on an x-ray spectrum with or without Ag Kα and Kβ, which is below 100 keV. Thus, a slight variation of the high-energy x-ray spectrum due to the divergence angle does not affect transmission calculations within our experimental condition.

IV. PHITS Monte Carlo modeling for broadband x-ray radiography

Calculated broadband x-ray spectra from LSP are used in the PHITS Monte Carlo code to simulate transmission profiles of the Al wires. Figure 4 shows a setup of the PHITS simulation in the experimental scale. A beam of photons spatially distributed over a Gaussian profile is injected in a plane at -21.6 cm. A solid density Al wire is placed at Z=0 and a 10 mm CH filter is in front of the Al wire, closer to the x-ray source in Fig. 4(c). Photons from the x-ray source transmit through both CH filter and Al wire and are deposited in a phosphor layer of an Image plate (BAS MS-type)[47]. The intensity dose deposited in the IP is divided by the intensity recorded outside the Al wire to calculate 1D transmission profiles shown in Fig. 4(d). The beam of photons diverges at 0.5° to form a magnified transmitted image of the Al wire at the IP position.

It is instructive to illustrate the relationship between the shape of transmission profiles and the source sizes. Figure 5 shows calculated transmission profiles of a 1mm diameter Al wire with various source sizes. The x-ray source is defined as a diameter of a Gaussian profile in FWHM, D, and varied from 0.2 to 2.0 mm. Variation of the x-ray source size primarily changes the opening of the transmission profile except the case for D=2.0 mm. The value of the transmission, on the other hand, is mainly determined by the x-ray source spectrum as shown later in Fig. 6. Therefore, the source size and x-ray spectrum in the simulations can be uniquely determined by comparing to measurements if the source is not significantly larger than the object size.

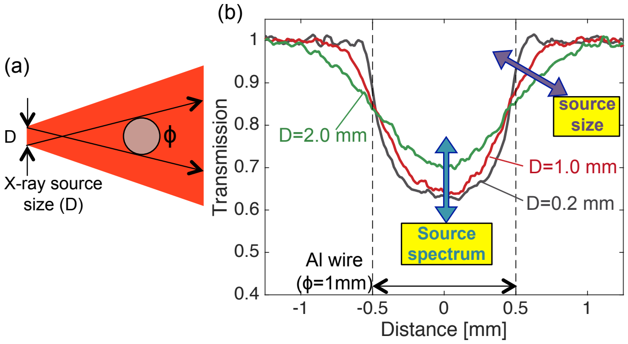

Figure 5 (a) A schematic of the relationship between the x-ray source size and object diameter. (b) Calculated transmission profiles of a 1.0 mm Al wire with the source sizes of 0.2, 1.0 and 2.0 mm diameter.

PHITS simulations with various source spectra and source sizes are performed to match the measured transmission profiles. Figure 6 compares the measured and simulated transmission profiles for 0.5, 1.0 and 1.6 mm diameter Al wires at IP 1. For each Al wire diameter, simulations are run using x-ray sources of 22 keV Ag Kα, LSP-calculated spectrum with T_{hot} = 0.50 MeV and θ =15° and an exponential x-ray spectrum with 80 keV as shown in Fig. 3(b). The measurements for the three cases agree with the simulations using the LSP spectrum composed of both

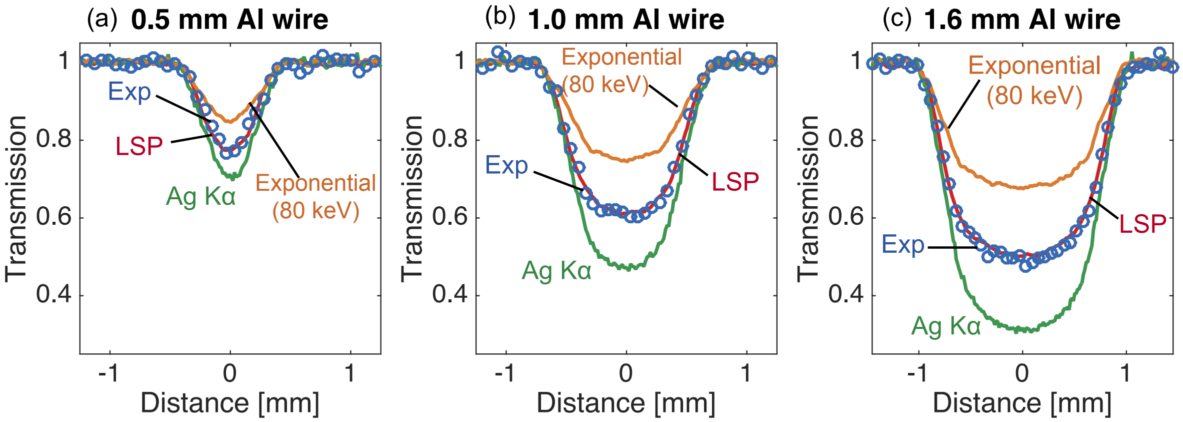

Figure 6 Comparisons of measured transmission profiles with PHITS calculations for (a) 0.5 mm, (b) 1.0 mm, and (c) 1.6 mm diameter Al wires. Three PHITS simulations are performed for each case with x-ray spectrum from LSP, monochromatic 22 keV Ag Kα, and an exponential spectrum with a slope temperature of 80 keV.

line emissions and bremsstrahlung. The intensity of the Ag Kα is the strongest in the spectrum. However, the photon sensitivity of IP is nearly constant between 10 and 100 keV and monotonically decreases by a factor of ~250 at 1 MeV.[46] Thus, it is critical to include the contribution of bremsstrahlung, particularly up to ~ 100 keV for transmission calculation for broadband x-ray radiographs.

Figure 7 shows comparisons of the transmission calculations with various source sizes for the 1 mm Al wire. It is shown that the source sizes with 200 µm and 1000 µm are narrower and wider than the measurement. In Fig.7 (b), the calculations with the source size of 400 and 800 µm reasonably bound the measurement so that the source size is determined to be 600 ± 200 µm. Similar source sizes are deduced for 25 and 100 µm thick Ag source foils. This relatively large source size estimated is comparable to the target foil size, specifically the height of the foil (in the X direction) as shown in Fig.1 (c). Since the target is a standalone thin foil mounted on a thin glass stalk, x-ray production is likely dominated by recirculation of fast electrons around the foil. Our result confirms that the broadband x-ray source that produced the radiographs of the Al wires is extended to the entire foil height. For further confirmation, the size of hard x-ray sources can be experimentally determined using penumbral imaging.[48,49,50]

To reduce the source size, we used a 25 µm diameter Ag wire target (X = 25 µm) placed parallel to the Al wire direction during the same experimental campaign. Indeed, the measured transmission profiles of the Al wires shows sharper edges compared to ones with the foil targets. A simulation for x-ray spectrum from a wire target, which requires a LSP simulation in a 3D geometry, is currently underway.

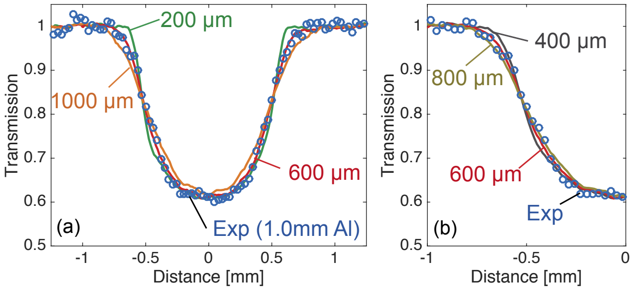

Figure 7 Comparisons of the measured transmission profile for 1mm Al wire with LSP-PHITS simulations using the source sizes of (a) 200, 600 and 1000 µm and (b) 400, 600 and 800 µm.

V. Application of broadband x-ray radiography in a pulsed power system

The coupled capability at the NTF allows the Leopard laser beam from the compressor to transport through a 3-m transport tube into the Zebra pulsed power chamber. Figure 8(a) shows a CAD model of the Zebra vacuum chamber for a coupled experiment. The beam sent down normal to the chamber is focused with a 90° gold OAP mirror. A 1150 µm diameter Al wire load coated with a 25 µm thick CH layer was positioned in the chamber center, while a 10 µm thick Ag backlighter foil is positioned at ~5.6 cm away from the center. A 10 mm thick CH filter and an IP were positioned in the same line of sight, but in the opposite side to the Ag foil at ~20 cm. The magnification of the point projection imaging geometry was ~3.6. The same electron spectrometer fielded in the laser experiment was used in the pulsed power chamber to measure escaping fast electrons above 1 MeV.

To demonstrate the generation of broadband x rays and radiography of a cold, solid Al wire in the Zebra chamber, the wire was not driven by a current in this experiment. Figure 8(b) and (c) show a radiograph of the cold Al wire recorded in the Zebra chamber and the transmission profile obtained from the radiographic image. We have successfully recorded radiographs of the Al wire on total 4 shots. On this particular shot (shot18), the electron signals recorded with the spectrometer were below 1 MeV, indicating that the on-target intensity was at the threshold of or lower than the relativistic intensity. The transmission

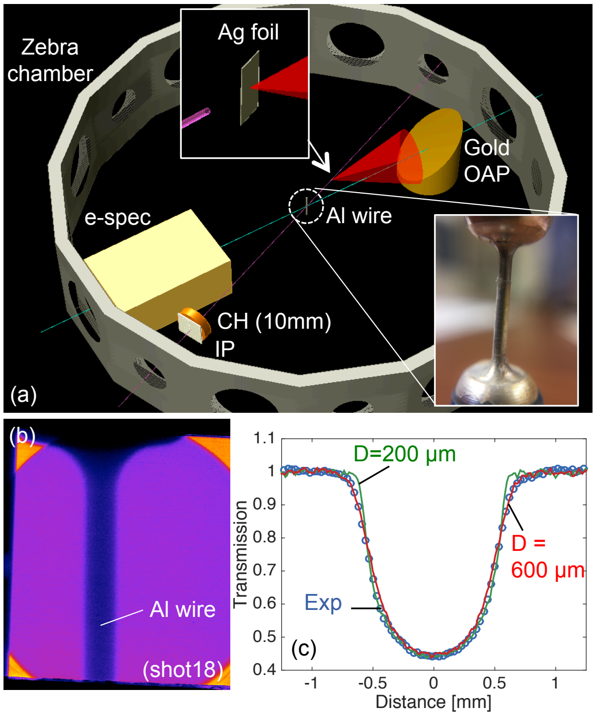

Figure 8 (a) A CAD drawing of the Zebra chamber coupled with the Leopard laser beam for broadband x-ray radiography experiment. (b) A radiograph of a 1 mm diameter Al wire in the Zebra chamber. (c) A transmission profile from the image in Fig. 8(b) and PHITS simulations using Ag Ka line emission and source sizes of D=200 and 600 um.

of the Al wire becomes lower than that observed in the laser chamber [see Fig. 6(b)]. A simulation using only Ag Kα line reproduces the value of 0.45 in transmission. To reproduce the full transmission profile, the source size of 200 and 600 μm is required. On the other shots, the peak transmission varies from 0.45 to 0.65. This implies that the on-target laser intensity, which is sensitive to accuracy and reproducibility of the target positioning, significantly varies so that the source spectrum was not well reproduced. In addition, the accurate control of the orientation of the foil is critical to obtain consistent source sizes. The projected length and orientation of the foil strongly affects the source size in the present geometry. The lower intensity on target could also be attributed to lower laser energy delivered to the target in the Zebra chamber due to the use of the Au parabolic mirror and the longer transport path with additional mirrors. To improve the reproducibility of x-ray source spectrum, a new target positioning system has been designed for future radiography experiments in the Zebra chamber.

VI. Conclusion

Broadband x rays produced by irradiating a silver foil with a Leopard short-pulse laser were characterized and applied for radiography of solid Al wires. Angularly resolved broadband spectra were determined in simultaneous fits to measured bremsstrahlung at two angular positions with hybrid-PIC LSP simulations. Comparisons of transmission of Al wires with PHITS model show good agreement when using the simulated x-ray spectrum and a source size of 600 ± 200 μm. The source size determined is comparable to the size of the target foil, indicating that the broadband x-ray source used for radiography is originated from the entire foil due to fast electron recirculation. The broadband x-ray radiography developed in this work could be applied for probing a magnetically driven metal cylinder in laser-pulsed power coupled experiments.

Acknowledgement

The authors would like to acknowledge Dr. P. Wiewior and O. Chalyy for their support of the Leopard laser operations, A. Astanovitskiy, O. Dmitriev and V. Nalajala, for conducting the experiment, and the NTF management for allocation of the experimental time. This work was supported by the National Science Foundation under Grant No. 1707357. This collaborative work was partially supported under the auspices of the U.S. Department of Energy by Lawrence Livermore National Laboratory under Contracts Nos. DE- AC52-07NA27344 and DEFG-02-05ER54834 (ACE).

---

[1] D. Umstadter, J. Workman, A. Maksimchuk, X. Liu, U. Ellenberger, J.S. Coe, and C.-Y. Chien, J. Quant. Spectrosc. Radiat. Transf. 54, 401 (1995).

[2] M.D. Perry, J.A. Sefcik, T. Cowan, S. Hatchett, A. Hunt, M. Moran, D. Pennington, R. Snavely, and S.C. Wilks, Rev. Sci. Instrum. 70, 265 (1999).

[3] R.D. Edwards, M.A. Sinclair, T.J. Goldsack, K. Krushelnick, F.N. Beg, E.L. Clark, A.E. Dangor, Z. Najmudin, M. Tatarakis, B. Walton, M. Zepf, K.W.D. Ledingham, I. Spencer, P. A. Norreys, R.J. Clarke, R. Kodama, Y. Toyama, and M. Tampo, Appl. Phys. Lett. 80, 2129 (2002).

[4] H.-S. Park, N. Izumi, M.H. Key, J.A. Koch, O.L. Landen, P.K. Patel, T.W. Phillips, and B.B. Zhang, Rev. Sci. Instrum. 75, 4048 (2004).

[5] K. Yasuike, M.H. Key, S.P. Hatchett, R. A. Snavely, and K.B. Wharton, Rev. Sci. Instrum. 72, 1236 (2001).

[6] R. Stephens, R. Snavely, Y. Aglitskiy, F. Amiranoff, C. Andersen, D. Batani, S. Baton, T. Cowan, R. Freeman, T. Hall, S. Hatchett, J. Hill, M. Key, J. King, J. Koch, M. Koenig, a. MacKinnon, K. Lancaster, E. Martinolli, P. Norreys, E. Perelli-Cippo, M. Rabec Le Gloahec, C. Rousseaux, J. Santos, and F. Scianitti, Phys. Rev. E 69, 066414 (2004).

[7] C. D. Chen, P. K. Patel, D. S. Hey, A. J. Mackinnon, M. H. Key, K. U. Akli, T. Bartel, F. N. Beg, S. Chawala, H. Chen et al., Phys. Plasmas 16, 082705 (2009).

[8] B. Westover, C. D. Chen, P. K. Patel, M. H. Key, H. McLean, R. Stephens, and F. N. Beg, Phys. Plasmas 18, 063101 (2011).

[9] M.N. Quinn, X.H. Yuan, X.X. Lin, D.C. Carroll, O. Tresca, R.J. Gray, M. Coury, C. Li, Y.T. Li, C.M. Brenner, A. P.L. Robinson, D. Neely, B. Zielbauer, B. Aurand, J. Fils, T. Kuehl, and P. McKenna, Plasma Phys. Control. Fusion 53, 025007 (2011).

[10] R.H.H. Scott, E.L. Clark, F. Pérez, M.J. V. Streeter, J.R. Davies, H.-P. Schlenvoigt, J.J. Santos, S. Hulin, K.L. Lancaster, S.D. Baton, S.J. Rose, and P.A. Norreys, Rev. Sci. Instrum. 84, 083505 (2013).

[11] H. Sawada, Y. Sentoku, A. Bass, B. Griffin, R. Pandit, F. Beg, H. Chen, H. McLean, A.J. Link, P.K. Patel, and Y. Ping, J. Phys. B At. Mol. Opt. Phys. 48, 224008 (2015).

[12] H. Chen, S. C. Wilks, D. D. Meyerhofer, J. Bonlie, C. D. Chen, S. N. Chen, C. Courtois, L. Elberson, G. Gregori, W. Kruer, O. Landoas, J. Mithen, J. Myatt, C. D. Murphy, P. Nilson, D. Price, M. Schneider, R. Shepherd, C. Stoeckl, M. Tabak, R. Tommasini, and P. Beiersdorfer, Phys. Rev. Lett. 105, 015003 (2010)

[13] R.J. Clarke, D. Neely, R.D. Edwards, P.N.M. Wright, K.W.D. Ledingham, R. Heathcote, P. McKenna, C.N. Danson, P.A. Brummitt, J.L. Collier, P.E. Hatton, S.J. Hawkes, C. Hernandez-Gomez, P. Holligan, M.H.R. Hutchinson, A.K. Kidd, W.J. Lester, D.R. Neville, P.A. Norreys, D.A. Pepler, T.B. Winstone, R.W.W. Wyatt, and B.E. Wyborn, J. Radiol. Prot. 26, 277 (2006).

[14] C.M. Brenner, S.R. Mirfayzi, D.R. Rusby, C. Armstrong, A. Alejo, L.A. Wilson, R. Clarke, H. Ahmed, N.M.H. Butler, D. Haddock, A. Higginson, A. McClymont, C. Murphy, M. Notley, P. Oliver, R. Allott, C. Hernandez-Gomez, S. Kar, P. McKenna, and D. Neely, Plasma Phys. Control. Fusion 58, 014039 (2016).

[15] R. Tommasini, S.P. Hatchett, D.S. Hey, C. Iglesias, N. Izumi, J. A. Koch, O.L. Landen, A. J. MacKinnon, C. Sorce, J. A. Delettrez, V.Y. Glebov, T.C. Sangster, and C. Stoeckl, Phys. Plasmas 18, 056309 (2011).

[16] C. Courtois, R. Edwards, A. Compant La Fontaine, C. Aedy, S. Bazzoli, J.L. Bourgade, J. Gazave, J.M. Lagrange, O. Landoas, L. Le Dain, D. Mastrosimone, N. Pichoff, G. Pien, and C. Stoeckl, Phys. Plasmas 20, 083114 (2013).

[17] C.P. Jones, C.M. Brenner, C.A. Stitt, C. Armstrong, D.R. Rusby, S.R. Mirfayzi, L.A. Wilson, A. Alejo, H. Ahmed, R. Allott, N.M.H. Butler, R.J. Clarke, D. Haddock, C. Hernandez-Gomez, A. Higginson, C. Murphy, M. Notley, C. Paraskevoulakos, J. Jowsey, P. McKenna, D. Neely, S. Kar, and T.B. Scott, J. Hazard. Mater. 318, 694 (2016).

[18] S. Palaniyappan, D.C. Gautier, B.J. Tobias, J.C. Fernandez, J. Mendez, T. Burris-Mog, C.K. Huang, A. Favalli, J.F. Hunter, M.E. Espy, D.W. Schmidt, R.O. Nelson, A. Sefkow, T. Shimada, and R.P. Johnson, Laser Part. Beams 1 (2019).

[19] J.A. King, K. Akli, B. Zhang, R.R. Freeman, M.H. Key, C.D. Chen, S.P. Hatchett, J. a. Koch, A.J. MacKinnon, P.K. Patel, R. Snavely, R.P.J. Town, M. Borghesi, L. Romagnani, M. Zepf, T. Cowan, H. Habara, R. Kodama, Y. Toyama, S. Karsch, K. Lancaster, C. Murphy, P. Norreys, R. Stephens, and C. Stoeckl, Appl. Phys. Lett. 86, 191501 (2005).

[20] B. Vauzour, F. Pérez, L. Volpe, K. Lancaster, P. Nicolaï, D. Batani, S.D. Baton, F.N. Beg, C. Benedetti, E. Brambrink, S. Chawla, F. Dorchies, C. Fourment, M. Galimberti, L.A. Gizzi, R. Heathcote, D.P. Higginson, S. Hulin, R. Jafer, P. Köster, L. Labate, A.J. MacKinnon, A.G. MacPhee, W. Nazarov, J. Pasley, C. Regan, X. Ribeyre, M. Richetta, G. Schurtz, A. Sgattoni, and J.J. Santos, Phys. Plasmas 18, 043108 (2011).

[21] W. Theobald, A. A. Solodov, C. Stoeckl, K. S. Anderson, F. N. Beg, R. Epstein, G. Fiksel, E. M. Giraldez, V. Y. Glebov, H. Habara, S. Ivan- cic, L. C. Jarrott, F. J. Marshall, G. McKiernan, H. S. McLean, C. Mileham, P. M. Nilson, P. K. Patel, F. Pérez, T. C. Sangster, J. J. Santos, H. Sawada, A. Shvydky, R. B. Stephens, and M. S. Wei, Nat. Commun. 5, 5785 (2014)

[22] C. Stoeckl, M. Bedzyk, G. Brent, R. Epstein, G. Fiksel, D. Guy, V. N. Gon- charov, S. X. Hu, S. Ingraham, D. W. Jacobs-Perkins, R. K. Jungquist, F. J. Marshall, C. Mileham, P. M. Nilson, T. C. Sangster, M. J. Shoup, and W. Theobald, Rev. Sci. Instrum. 85, 11E501 (2014).

[23] D.T. Casey, D.T. Woods, V.A. Smalyuk, O.A. Hurricane, V.Y. Glebov, C. Stoeckl, W. Theobald, R. Wallace, A. Nikroo, M. Schoff, C. Shuldberg, K.J. Wu, J.A. Frenje, O.L. Landen, B.A. Remington, and G. Glendinning, Phys. Rev. Lett. 114, 205002 (2015).

[24] H. Sawada, S. Lee, T. Shiroto, H. Nagatomo, Y. Arikawa, H. Nishimura, T. Ueda, K. Shigemori, A. Sunahara, N. Ohnishi, F. N. Beg, W. Theobald, F. Pérez, P. K. Patel, and S. Fujioka, Appl. Phys. Lett. 108, 254101 (2016).

[25] M. S. Schollmeier and G. P. Loisel, Rev. Sci. Instrum. 87, 123511 (2016).

[26] R. Tommasini, C. Bailey, D.K. Bradley, M. Bowers, H. Chen, J.M. Di Nicola, P. Di Nicola, G. Gururangan, G.N. Hall, C.M. Hardy, D. Hargrove, M. Hermann, M. Hohenberger, J.P. Holder, W. Hsing, N. Izumi, D. Kalantar, S. Khan, J. Kroll, O.L. Landen, J. Lawson, D. Martinez, N. Masters, J.R. Nafziger, S.R. Nagel, A. Nikroo, J. Okui, D. Palmer, R. Sigurdsson, S. Vonhof, R.J. Wallace, and T. Zobrist, Phys. Plasmas 24, 053104 (2017).

[27] P.P. Wiewior, V. V Ivanov, and O. Chalyy, J. Phys. Conf. Ser. 244, 032013 (2010).

[28] R. Presura, C. Plechaty, D. Martinez, M.S. Bakeman, P.J. Laca, C. Haefner, A.L. Astanovitskiy, and M. Thompson, IEEE Trans. Plasma Sci. 36, 17 (2008).

[29] V. V. Ivanov, P. Hakel, R.C. Mancini, J.P. Chittenden, A. Anderson, T. Durmaz, P. Wiewior, D. Papp, S.D. Altemara, A. L. Astanovitskiy, and O. Chalyy, Phys. Rev. Lett. 106, 225005 (2011).

[30] V. V. Ivanov, A. V. Maximov, R. Betti, L.S. Leal, R.C. Mancini, K.J. Swanson, I.E. Golovkin, C.J. Fontes, H. Sawada, A.B. Sefkow, and N.L. Wong, Phys. Plasmas 26, 062707 (2019).

[31] D. Mariscal, C. McGuffey, J. Valenzuela, M.S. Wei, J.P. Chittenden, N. Niasse, R. Presura, S. Haque, M. Wallace, A. Arias, A. Covington, H. Sawada, P. Wiewior, and F.N. Beg, Appl. Phys. Lett. 105, 224103 (2014).

[32] H. Sawada, T. Daykin, B. Bauer, and F. Beg, in APS Division of Plasma Physics Meeting (2017), abstract id. NO6.002.

[33] C.A. Hall, Phys. Plasmas 7, 2069 (2000).

[34] H. Sawada, Y. Sentoku, T. Yabuuchi, U. Zastrau, E. Förster, F.N. Beg, H. Chen, A.J. Kemp, H.S. McLean, P.K. Patel, and Y. Ping, Phys. Rev. Lett. 122, 155002 (2019).

[35] C. D. Chen, J. A. King, M. H. Key, K. U. Akli, F. N. Beg, H. Chen, R. R. Freeman, A. Link, A. J. Mackinnon, A. G. MacPhee, P. K. Patel, M. Porkolab, R. B. Stephens, and L. D. Van Woerkom, Rev. Sci. Instrum. 79, 10E305 (2008).

[36] H. Chen, P. K. Patel, D. F. Price, B. K. Young, P. T. Springer, R. Berry, R. Booth, C. Bruns, and D. Nelson, Rev. Sci. Instrum. 74, 1551 (2003)

[37] A. Link, R. R. Freeman, D. W. Schumacher, and L. D. Van Woerkom, Phys. Plasmas 18, 053107 (2011).

[38] O.L. Landen, D.R. Farley, S.G. Glendinning, L.M. Logory, P.M. Bell, J.A. Koch, F.D. Lee, D.K. Bradley, D.H. Kalantar, C.A. Back, and R.E. Turner, Rev. Sci. Instrum. 72, 627 (2001).

[39] N.L. Kugland, C.G. Constantin, T. Döppner, P. Neumayer, S.H. Glenzer, and C. Niemann, J. Instrum. 6, T03002 (2011).

---

[40] C. D. Chen, Ph.D thesis, PSFC/RR-09-4 (2009)

[41] T.S. Daykin, H. Sawada, Y. Sentoku, F.N. Beg, H. Chen, H.S. McLean, A.J. Link, P.K. Patel, and Y. Ping, Phys. Plasmas **25**, 123103 (2018).

[42] D. Welch, D. Rose, B. Oliver, and R. Clark, Nucl. Instrum. Methods Phys. Res., Sect. A 464, 134 (2001)

[43] T. Sato, Y. Iwamoto, S. Hashimoto, T. Ogawa, T. Furuta, S. Abe, T. Kai, P.-E. Tsai, N. Matsuda, H. Iwase, N. Shigyo, L. Sihver, and K. Niita, J. Nucl. Sci. Technol. 55, 684 (2018).

[44] J. A. Halbleib, R. P. Kensek, T. A. Mehlhorn, G. D. Valdez, S. M. Seltzer, and M. J. Berger, Sandia National Laboratories Technical Report No. SAND91-1634, 1992.

[45] A. L. Meadowcroft, C.D. Bentley, and E.N. Stott, Rev. Sci. Instrum. **79**, 2 (2008).

[46] T. Bonnet, M. Comet, D. Denis-Petit, F. Gobet, F. Hannachi, M. Tarisien, M. Versteegen, and M.M. Aléonard, Rev. Sci. Instrum. **84**, 0 (2013).

[47] Y. Amemiya, T. Matsushita, A. Nakagawa, Y. Satow, J. Miyahara, and J. Chikawa, Nucl. Instruments Methods Phys. Res. Sect. A Accel. Spectrometers, Detect. Assoc. Equip. 266, 645 (1988).

[48] R. A. Richardson and T. L. Houck, “Roll bar x-ray spot size measurement technique”, No. UCRL-JC—130427, pp 908–910 (1998)

[49] C. Courtois, a. Compant La Fontaine, O. Landoas, G. Lidove, V. Méot, P. Morel, R. Nuter, E. Lefebvre, a. Boscheron, J. Grenier, M.M. Aléonard, M. Gerbaux, F. Gobet, F. Hannachi, G. Malka, J.N. Scheurer, and M. Tarisien, Phys. Plasmas 16, 013105 (2009).

[50] B. Bachmann, H. Abu-Shawareb, N. Alexander, J. Ayers, C. G. Bailey, P. Bell, L. R. Benedetti, D. Bradley, G. Collins, L. Divol, T. Döppner, S. Felker, J. Field, A. Forsman, J. D. Galbraith, C. M. Hardy, T. Hilsabeck, N. Izumi, C. Jarrot, J. Kilkenny, S. Kramer, O. L. Landen, T. Ma, A. MacPhee, N. Masters, S. R. Nagel, A. Pak, P. Patel, L. A. Pickworth, J. E. Ralph, C. Reed, J. R. Rygg, and D. B. Thorn "X-ray penumbral imaging diagnostic developments at the National Ignition Facility", Proc. SPIE 10390, Target Diagnostics Physics and Engineering for Inertial Confinement Fusion VI, 103900B (26 September 2017); doi: 10.1117/12.2274611; https://doi.org/10.1117/12.2274611